Response to Reviewer 2

Reviewer comments are quoted in italics, and our responses follow in regular font. After each response, we quote the new or changed text of the revised manuscript and Supplement. Line numbers in our responses refer to the revised manuscript with tracked changes; line numbers in the reviewer's comments refer to the initial submission.

> *The manuscript discusses a quite unexpected effect of a positive radiative forcing caused by a stratospheric aerosol layer under certain conditions, especially at small solar zenith angles above surfaces with high Lambertian albedo. Although this effect was already reported by other authors, they explained it with the aerosol absorption while the presented manuscript proofs that the effect is observable also for non-absorbing aerosols. Authors suggest a simple model, which helps to understand the obtained results. Furthermore, authors compare the two-stream approximation, commonly used by climate models, with the results from the 16 stream radiative transfer modeling using DISORT and report biases associated with the usage of the two-stream approximation. Although the study is quite simple, its results can be interesting for the scientific community. After some improvements the manuscript can be accepted for the publications.*

We thank the reviewer for the careful reading and constructive comments. In response, we added a check of the main conclusions with a standard molecular atmosphere (Comment 2), a closed-form forcing expression that gives the critical surface albedo for positive forcing as $1/\Phi$ (Comments 11 and 12), the missing model setup details (Comments 3, 4, 7 and 10), and the technical corrections.

While preparing this response, we found that some submitted figures had been produced with model settings from an earlier stage of the work. We regenerated these figures with the settings stated in Sect. 2 and corrected the affected numbers, as described under "Author-initiated corrections" at the end of this document.

Detailed comments

Comment 1

> *Line 76: Please remind the reader that Φ is the asymmetry factor.*

Φ is the reflectance asymmetry parameter, $\Phi = R\uparrow/R\downarrow$ (Eq. 8), not the phase function asymmetry factor g. $R\downarrow$ is the aerosol layer's reflectance for the direct solar beam, and $R\uparrow$ is its reflectance for diffuse light reflected by the surface. The submitted Introduction used Φ before its definition in Sect. 4.3; we now define it at its first appearance.

Revised manuscript, lines 76–80:

> We test the robustness of this mechanism using the reflectance asymmetry parameter Φ, defined as the ratio of the layer's reflectance for diffuse light reflected by the surface to its reflectance for the direct beam (Sect. 4). Numerical radiative transfer simulations confirm that this parameter depends on solar geometry and is independent of the underlying surface albedo.

Comment 2

> *Section 2.1: Adequacy of the single-layer radiative transfer model with no background atmospheric molecular scattering or absorption needs to be discussed in more details.*

Positive forcing over bright surfaces at small SZA persists with a molecular atmosphere, and DISORT still gives a larger positive forcing than RODENTS. The main simulations exclude the molecular atmosphere to isolate scattering by the aerosol layer. We agree that the submitted text did not show that the conclusions hold with a molecular atmosphere. We therefore repeated the calculations of Fig. 1 and the daily means of Fig. 2 for both solvers with the US standard atmosphere, including Rayleigh scattering and gaseous absorption. The molecular atmosphere raises the critical surface albedo (from 0.32 to 0.44 at SZA = 5°) and lowers the peak forcing (from +3.1 to +2.0 W m^{-2}). With the molecular atmosphere, the daily-mean ADRF remains negative at every surface albedo in all three latitude bands. The statement in Sect. 3 that the daily mean becomes positive at very high surface albedo therefore holds only without the molecular atmosphere; the revised Sect. 3 states this.

Revised manuscript, lines 101–104:

> We excluded background atmospheric molecular scattering and absorption from the main simulations to isolate scattering by the aerosol layer. Their effects are assessed in Sect. 5 and in Sect. S8 of the Supplement.

Revised manuscript, lines 220–221:

> With the molecular atmosphere of Sect. S8, the daily-mean ADRF remains negative at every surface albedo in all three bands (−0.5 W m^{-2} at A_s = 1 in the tropics).

Revised manuscript, lines 228–229:

> With the molecular atmosphere, this reversal persists and extends to $A_s \lesssim 0.7$ (Sect. S8).

Revised manuscript, lines 452–458:

> The main simulations exclude background atmospheric molecular scattering and absorption to isolate scattering by the aerosol layer. The absolute magnitudes of ADRF reported here should therefore be interpreted as indicative of trends rather than quantitative predictions. With the US standard atmosphere included (Sect. S8), the forcing remains positive over bright surfaces at small SZA and the solver difference persists. The critical surface albedo rises (from 0.32 to 0.44 at SZA = 5°), and the peak forcing decreases (from +3.1 to +2.0 W m^{-2}).

Revised Supplement, new Sect. S8:

> **S8 Effect of a molecular atmosphere**

The simulations of the main text contain no molecular scattering or absorption, so the computed forcing and reflectance asymmetry are those of the aerosol layer alone (Sect. 2.1). To check whether the conclusions hold in a molecular atmosphere, we repeated the calculations of Fig. 1 using the US standard atmosphere of libRadtran (Anderson et al., 1986). This includes Rayleigh scattering and gaseous absorption by water vapor, ozone, oxygen, carbon dioxide and the trace gases. The gaseous absorption is parameterized with the LOWTRAN band model (Pierluissi and Peng, 1985) as adopted from SBDART (Ricchiazzi et al., 1998). All other settings are unchanged (Mie optical properties, a wavelength range of 250–3000 nm, an aerosol layer at 18–24 km, DISORT with 16 streams and RODENTS, and surface albedo from 0 to 1 in steps of 0.05). The ADRF is again the difference between the upward TOA irradiances without and with the aerosol layer, both computed with the molecular atmosphere. Figure S8 and Table S6 compare the two configurations.

The forcing retains the same sign pattern as without the molecular atmosphere. The ADRF is negative over low-albedo surfaces and becomes positive above a critical surface albedo at small SZA. It remains negative at every surface albedo for SZA ≥ 65°. Wherever the forcing is positive, DISORT gives a larger positive forcing than RODENTS. With the molecular atmosphere, the critical surface albedo rises (DISORT: from 0.32 to 0.44 at SZA = 5°, from 0.37 to 0.51 at 25° and from 0.57 to 0.77 at 45°). The positive peak decreases and moves to a higher surface albedo (from +3.1 W m^{-2} at A_s = 0.65 to +2.0 W m^{-2} at A_s = 0.80 at SZA = 5°, and from +2.3 to +1.5 W m^{-2} at 25°). The cooling over a black surface is reduced (by 13 % at SZA = 5° and by 44 % at 85°). At A_s = 1, the forcing no longer vanishes (+1.4 W m^{-2} at SZA = 5° and −5.0 W m^{-2} at 85°).

We also recomputed the daily means of Fig. 2 with the molecular atmosphere for all nine SZA bins and both solvers. The daily means remain negative at every surface albedo in all three latitude bands (DISORT at A_s = 1: −0.5 W m^{-2} in the tropics, −0.7 W m^{-2} at midlatitudes and −2.0 W m^{-2} in the polar band). Without the molecular atmosphere, the DISORT daily means become positive at $A_s \geq 0.74$ in the tropics and at $A_s \geq 0.83$ at midlatitudes (maxima +0.3 and +0.1 W m^{-2}) and remain at or below zero in the polar band. The statement in Sect. 3 that the daily mean becomes positive at very high surface albedo therefore does not hold with the molecular atmosphere. The reversal of the solver bias at low surface albedo in the polar band persists. Its range extends from $A_s \lesssim 0.4$ to $A_s \lesssim 0.7$. The low-albedo range in which RODENTS is less negative than DISORT in the tropics and at midlatitudes widens from $A_s \leq$ 0.05–0.1 to $A_s \leq$ 0.2–0.25.

Table S6. The table compares instantaneous ADRF without (first value, the configuration of the main text) and with (second value) the US standard molecular atmosphere, for purely scattering alumina (Mie optical properties, 250–3000 nm). The critical A_s is the surface albedo at which the ADRF changes sign (linear interpolation on the 0.05 grid); "none" means that the ADRF is negative at every $A_s < 1$.

SZA	Solver	ADRF at A_s = 0 (W m^{-2})	Critical A_s (ADRF = 0)	Peak ADRF (W m^{-2}) and its A_s	ADRF at A_s = 1 (W m^{-2})
5°	DISORT	−8.14 / −7.09	0.32 / 0.44	+3.06 (0.65) / +2.03 (0.80)	0.00 / +1.41

5°	RODENTS	−8.44 / −7.15	0.50 / 0.57	+1.08 (0.75) / +0.88 (0.85)	0.00 / +0.56
25°	DISORT	−8.74 / −7.57	0.37 / 0.51	+2.34 (0.70) / +1.50 (0.85)	0.00 / +1.12
25°	RODENTS	−9.24 / −7.82	0.60 / 0.71	+0.63 (0.80) / +0.38 (0.90)	0.00 / +0.24
45°	DISORT	−10.43 / −8.88	0.57 / 0.77	+0.86 (0.80) / +0.41 (0.95)	0.00 / +0.39
45°	RODENTS	−11.01 / −9.18	0.92 / none	+0.02 (0.95) / none	0.00 / −0.48
65°	DISORT	−14.02 / −11.29	none / none	none / none	0.00 / −1.12
65°	RODENTS	−13.40 / −10.53	none / none	none / none	0.00 / −1.67
85°	DISORT	−18.21 / −10.27	none / none	none / none	0.00 / −5.01
85°	RODENTS	−14.48 / −7.83	none / none	none / none	0.00 / −4.20

Revised Supplement, Fig. S8 and its caption:

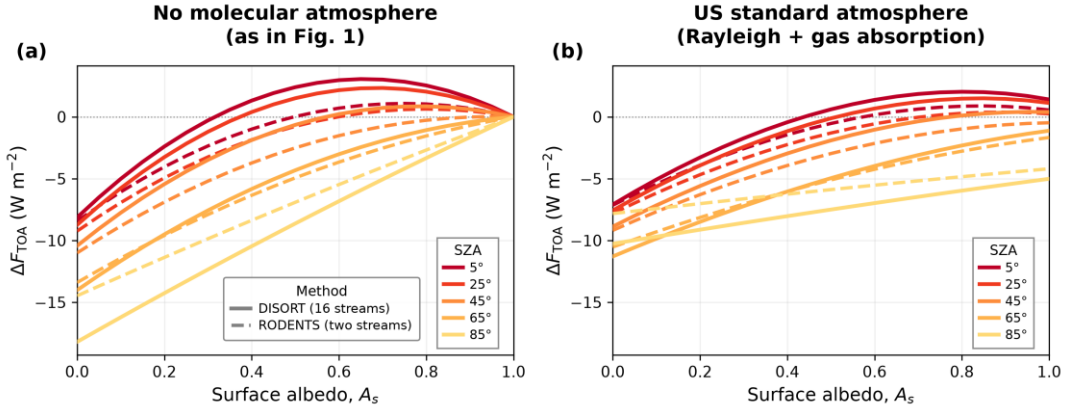


Figure S8. Instantaneous ADRF versus surface albedo for the purely scattering alumina layer (a) without a molecular atmosphere, as in Fig. 1, and (b) with the US standard atmosphere (Rayleigh scattering and gaseous absorption), computed with DISORT (16 streams, solid) and RODENTS (dashed) at five SZA values. The optical properties, the layer and the spectral range are the same as in Fig. 1.

Comment 3

Section 2.1: In radiative transfer publications the number of streams is often refers to a hemisphere. This means that the full number of streams for both upward and downward directions is double. Please clarify, if 16 streams used by you refer to the full sphere or to a hemisphere.

The 16 streams refer to the full sphere, following the definition in DISORT (Stamnes et al., 1988) and libRadtran (Emde et al., 2016). The code splits the 16 streams into eight per hemisphere. In the convergence test with 16, 32 and 64 streams, i.e., 8, 16 and 32 per hemisphere, Φ changed by at most 0.13 % and the ADRF by less than 0.01 W m^{-2} (see also our response to Comment 6).

Revised manuscript, lines 105–108:

> The RTE was solved using two methods to evaluate the impact of multiple scattering treatment on ADRF: (1) the Roberts Delta-Eddington Two-Stream solver (RODENTS), representative of the two-stream approximations employed in most general circulation models (Zdunkowski et al., 2007), and (2) the 16-stream DISORT solver (eight streams per hemisphere), which resolves the angular distribution of intensity with higher fidelity (Stamnes et al., 1988).

Comment 4

> *Line 103: Please precise how the instantaneous upward spectral irradiance was calculated in DISORT. Is it the radiance integrated over all directions or is it rather a flux, i.e. radiance weighted with cosine of the incidence angle?*

It is a flux: the upward irradiance is the radiance weighted by the cosine of the zenith angle and integrated over the upper hemisphere (the libRadtran output "eup"), not the actinic flux. The same definition applies to RODENTS and to the downward irradiance S(μ), so R↓ and R↑ are ratios of hemispheric fluxes.

Revised manuscript, lines 112–114:

> The solution to the RTE provides instantaneous upward spectral irradiance ($F\lambda\uparrow$) at the top of the atmosphere (TOA). This hemispheric flux is computed by weighting the upward radiance by the cosine of the zenith angle and integrating over the upper hemisphere; it is distinct from the actinic flux.

Comment 5

> *Section 2.2: Please discuss the adequacy of considering alumina particles spherical as required by the Mie calculations.*

We model the particles as homogeneous spheres, which serve as a reference particle shape, and compute their optical properties with Lorenz–Mie theory. Model simulations of alumina injection find that coagulation into non-spherical aggregates is minor for injected particle radii larger than about 200 nm under the conditions examined (Weisenstein et al., 2015; Vattioni et al., 2024). This is comparable to the median radius of our baseline distribution (215 nm; median diameter 430 nm). These simulations do not establish that aggregation is negligible in concentrated injection plumes. Spherical alumina particles have also been collected in the stratosphere and attributed to solid-rocket exhaust (Brownlee et al., 1976), although those particles (3–8 μm) were larger than ours. The revised Sects. 2.2 and 5 state this assumption and discuss how non-spherical shapes can affect the phase function, Φ and the forcing.

Revised manuscript, lines 120–130:

> We computed the aerosol optical properties required as input to the RTE – extinction coefficient, SSA, and scattering phase function – using Lorenz–Mie theory for homogeneous spherical particles, as implemented in the PyMieScatt Python library (Sumlin et al., 2018). Injected solid particles may coagulate into non-spherical aggregates, depending on particle size, concentration and injection conditions. Model simulations of

alumina injection find that this self-coagulation is minor for particle radii larger than about 200 nm under the conditions examined (Weisenstein et al., 2015; Vattioni et al., 2024), comparable to the median radius of the size distribution used here (215 nm; Sect. 2.1). These simulations do not establish that aggregation is negligible in concentrated injection plumes. Spherical alumina particles have also been collected in the stratosphere and attributed to solid-rocket exhaust (Brownlee et al., 1976), although these particles (3–8 μm) were larger than those considered here. The effect of particle shape is discussed in Sect. 5. Wavelength-dependent refractive indices of alumina from Tropf and Thomas (1997) were used as input, and the optical properties were calculated over the spectral range of 250 nm to 3000 nm.

Revised manuscript, lines 461–472:

The particles are modeled as homogeneous spheres (Sect. 2.2). Non-spherical particles, such as aggregates, have phase functions that differ from those of equivalent spheres. These differences can change $\beta(\mu)$ and, through it, Φ and the forcing. For the dust-like spheroids examined by Mishchenko et al. (1997), the asymmetry parameter and the backscattered fraction differ from those of equivalent spheres by less than about 10 % in most cases. This result was obtained for mineral dust and does not provide an error bound for alumina. When the phase function is approximated by its first two Legendre terms, the $\Phi = 1$ crossover lies at SZA = 60° for any asymmetry parameter (Eq. 15). The higher-order Legendre terms depend on particle shape, and quantifying their effect for alumina requires calculations for representative non-spherical particles. Shape and size are less certain for reentry-derived particles. Reentry metals have been observed within stratospheric sulfate particles (Murphy et al., 2023). Maloney et al. (2025) assumed initial alumina emission radii of 10 nm and 100 nm, and Ferreira et al. (2024) examined the formation of nanometer-scale alumina particles during reentry. These studies do not establish the size and shape of the particles after their subsequent atmospheric evolution. The homogeneous-sphere calculation is therefore an idealization for this source.

Comment 6

Section 2.2: If the total number of streams is 32, the number of Legendre moments of 17 is too low.

The total number of streams is 16 (eight per hemisphere), and the expansion supplied to DISORT contains 33 Legendre moments ($l = 0–32$). The submitted value of 17 was a textual error: it belonged to a different input option that does not affect irradiances. The error did not affect the calculations. With the delta-M scaling applied by DISORT (Wiscombe, 1977), a 16-stream irradiance calculation uses the first 17 of these moments. Comparisons with 32 and 64 streams support the use of 16 streams for this study (Sect. S3).

Revised manuscript, lines 131–140:

The scattering phase function was expanded in Legendre polynomials to provide the angular scattering representation required by DISORT. The expansion supplied to the solver contained 33 moments ($l = 0–32$), with Legendre coefficients computed following the pmom algorithm of libRadtran (Emde et al., 2016). Over all scattering angles, the largest

relative difference between the phase function reconstructed from these moments and the Mie phase function is 3.6 % at the shortest wavelength (250 nm) and below 0.01 % at 550 nm (Sect. S1). DISORT applies delta-M scaling (Wiscombe, 1977) by treating the narrow forward-scattering peak of the phase function as unscattered light. A 16-stream irradiance calculation then depends only on the first 17 moments. Calculations with 16, 32 and 64 streams differ by less than 0.15 % in Φ and by less than 0.01 W m^{-2} in the ADRF (Sect. S3). Details of the Legendre polynomial fitting procedure, including the normalization condition, recurrence relation, and numerical quadrature method, are provided in Sect. S1 of the Supplement.

Revised Supplement, Sect. S1, text after Eq. (S3):

for l = 0, 1, . . ., 32, where N = 90 and nmom = 33. The Legendre polynomials

Revised Supplement, Sect. S1, text after Eq. (S4):

starting from $P_0(\mu) = 1$ and $P_1(\mu) = \mu$. These moments were computed following the pmom function from libRadtran and written into the aerosol input file in the format required by libRadtran. Across all scattering angles, the largest relative difference between the phase function reconstructed from the 33 moments and the Mie phase function is 3.6 % at 250 nm, the shortest wavelength considered, and below 0.01 % at 550 nm.

Revised Supplement, new Sect. S3:

S3 Convergence with the number of DISORT streams

The phase-function expansion supplied to DISORT contained 33 Legendre moments (l = 0–32). DISORT applies delta-M scaling (Wiscombe, 1977), so a calculation with N streams uses only the first N + 1 moments. Higher-order moments do not change the computed irradiances. Convergence must therefore be tested by varying the number of streams. We computed a second set of 129 moments using Gauss–Legendre quadrature of the Mie phase function. Its first 33 moments differ from those used in the main text, which were computed with the trapezoidal rule (Sect. S1). The differences are less than 7×10^{-3}. Using this set, we repeated the broadband calculations for surface albedos of 0–0.9, with 16 and 32 streams at SZA = 5–85° and with 64 streams at SZA = 5°, 25°, 45°, 65° and 85°.

Increasing the number of streams from 16 to 32 changes the reflectance asymmetry parameter Φ by at most 0.13 %. Increasing it from 32 to 64 changes this parameter by at most 0.03 %. For each pair of calculations, we compared the instantaneous ADRF at every combination of SZA and surface albedo represented in both calculations. The largest difference is 0.008 W m^{-2} between 16 and 32 streams and 0.001 W m^{-2} between 32 and 64 streams (Table S1). The SZA at which $\Phi = 1$ shifts by 0.03° between 16 and 64 streams. With 16 streams, replacing the 33 moments of the main text with the 129-moment set changes Φ by at most 0.03 %. Because a 16-stream calculation uses only the first 17 moments, this small change comes from differences between the first 17 moments of the two sets, rather than from the additional moments. The 16-stream configuration used in the main text is therefore sufficient for the analysis presented in this study (Fig. S4, Table S1).

Table S1. Convergence of the DISORT calculations with the number of streams (Sect. S3). The table gives the largest changes over SZA = 5–85° (for 32 → 64 streams, at SZA = 5°,

25°, 45°, 65° and 85°) and surface albedos of 0–0.9 for the purely scattering alumina layer (250–3000 nm). F↑ is the upward irradiance at the TOA.

Comparison	max |ΔΦ/Φ|	max |ΔF↑/F↑|	max |ΔADRF|
33 vs. 129 moments (both 16 streams)	0.03 %	0.09 %	–
16 → 32 streams	0.13 %	0.023 %	0.008 W m^{-2}
32 → 64 streams	0.03 %	0.0002 %	0.001 W m^{-2}

Revised Supplement, Fig. S4 and its caption:

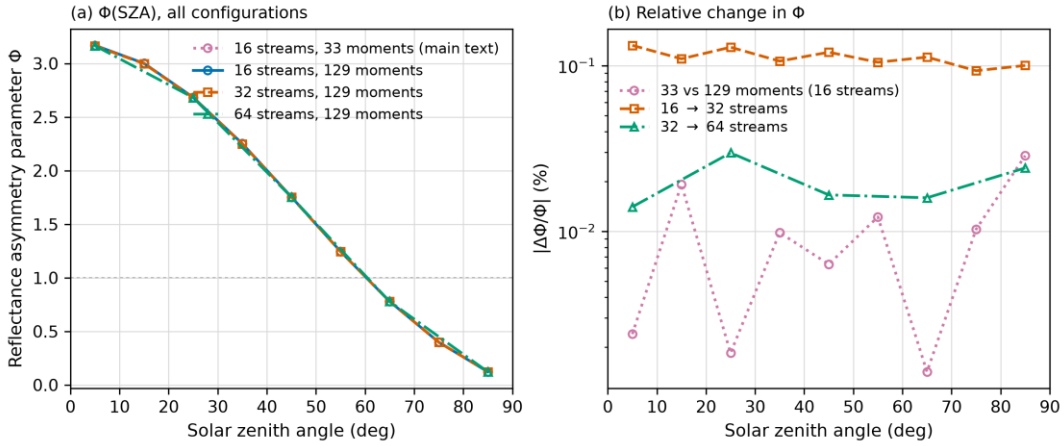


Figure S4. Convergence with the number of streams. Panel (a) shows Φ(SZA) computed with 16 streams and the 33 moments used in the main text, and with 16, 32 and 64 streams and the 129-moment set (64 streams only at SZA = 5°, 25°, 45°, 65° and 85°). The four curves coincide. Panel (b) shows the relative change in Φ between these calculations; all changes are below 0.15 %.

Comment 7

Section 2.3: Step size in the local time needs to be reported.

The diurnal cycle is sampled every 5 min (288 steps per day). At each daylight step, the ADRF is taken from the simulation at the center of the 10° SZA bin that contains the current SZA. Linear interpolation in SZA instead changes the daily means by less than 0.03 W m^{-2}.

Revised manuscript, lines 148–151:

We sampled the diurnal cycle every 5 min (288 steps per day). At each daylight step, we used the instantaneous ADRF simulated at the center of the 10° SZA bin containing θ(t) (SZA = 5°, 15°, …, 85°). Using linear interpolation in SZA instead changes the daily means by less than 0.03 W m^{-2}.

Comment 8

Lines 160–163: Please discuss what is new/different in this study with respect to (Randels et al., 2013).

Our study extends the comparison to bright surfaces, explains the positive forcing, and identifies the origin of the two-stream error. Randles et al. (2013) compared 31 radiation schemes with line-by-line benchmarks for a scattering aerosol at a surface albedo of 0.2 and SZA = 30° and 75°. Relative to the benchmarks, the various schemes overestimated cooling by about 20 % at 30° and underestimated it by about 10 % at 75°. Our comparison reproduces this pattern over a black surface ($A_s = 0$): RODENTS cools 4–6 % more than DISORT at SZA ≤ 45° and 13–20 % less at 75–85°.

(1) Over bright surfaces, the two-stream error is no longer a few percent of the cooling: RODENTS underestimates the positive forcing by more than half (+1.0 vs. +2.5 W m^{-2} at SZA = 5° and $A_s = 0.8$).

(2) We identify the mechanism of the positive forcing and its condition, $1/\Phi < A_s < 1$ (Sect. 4).

(3) We identify the origin of the two-stream error. Over a black surface, it comes from the layer's reflectance for the direct beam, R↓: RODENTS gives R↓ values 4–6 % higher than DISORT at SZA ≤ 45° and 20 % lower at 85°. Over bright surfaces, the error comes mainly from the reflectance for diffuse light from the surface, R↑, which RODENTS underestimates by 34 % at every SZA (Sect. 4.4).

Revised manuscript, lines 191–199:

> This pattern – two-stream methods overestimating cooling at low SZA and underestimating it at high SZA – is consistent with the findings of Randles et al. (2013), who compared 31 radiative transfer schemes with line-by-line benchmarks for a scattering aerosol over a surface of albedo 0.2. Relative to the benchmarks, the various schemes overestimated the cooling by about 20 % at SZA = 30° and underestimated it by about 10 % at 75°. That intercomparison used a single, low surface albedo. The present results extend the comparison to the full albedo range. The two-stream error grows from 4–6 % of the cooling over a black surface ($A_s = 0$) at SZA ≤ 45° to more than half of the positive forcing over bright surfaces (RODENTS gives +1.0 W m^{-2} compared with +2.5 W m^{-2} for DISORT at SZA = 5° and $A_s = 0.8$). Section 4.4 attributes this error to the response of the layer to diffuse light.

Comment 9

> *Figure 2 caption: "Figure 2a, b and c" – I think you mean "Figure 2b, c and d", panel a is not described.*

We corrected the caption.

Revised manuscript, lines 204–211:

> **Figure 2.** Daily-mean ADRF at the effective latitude of each latitude band, as a function of the prescribed uniform surface albedo A_s. The method for calculating this averaged ADRF is described in Sect. 2.3. Figure 2a shows the diurnal cycle of SZA for the three latitude bands; Fig. 2b, c and d respectively represent the daily-mean ADRF in the tropics, midlatitudes and polar region on the summer-solstice day in the northern hemisphere. The solid lines represent DISORT 16 streams solver and dashed lines represent RODENTS two

streams solver. The shaded blue areas represent the area-weighted frequency distributions of the MODIS surface albedo in the corresponding latitude bands (June–August 2025); they are shown for reference and do not enter the averaging.

Comment 10

Figure 2: It is unclear why ΔF is a function of the surface albedo. The integration over the latitude bin is already done and should consider the distribution of the surface albedo or was the integration done for set of assumed constant albedos?

The daily means were computed for a set of assumed constant surface albedos, extending the instantaneous results of Fig. 1 to a full day (Fig. 2). Each point on the curves in Fig. 2b–d uses one prescribed, uniform surface albedo (the abscissa). The instantaneous ADRF is averaged over the daily cycle of SZA at the band's effective latitude, without averaging over the band's surface albedo distribution. The MODIS albedo distribution (blue shading) is shown for reference and does not enter the averaging. We reworded the caption and Sect. 2.3 to state this explicitly.

Revised manuscript, lines 151–152:

For each prescribed, uniform surface albedo A_s, we computed a separate daily mean by averaging the ADRF over the daily cycle of SZA, without averaging over the surface albedo distribution within the latitude band.

Revised manuscript, lines 204–211:

Figure 2. Daily-mean ADRF at the effective latitude of each latitude band, as a function of the prescribed uniform surface albedo A_s. The method for calculating this averaged ADRF is described in Sect. 2.3. Figure 2a shows the diurnal cycle of SZA for the three latitude bands; Fig. 2b, c and d respectively represent the daily-mean ADRF in the tropics, midlatitudes and polar region on the summer-solstice day in the northern hemisphere. The solid lines represent DISORT 16 streams solver and dashed lines represent RODENTS two streams solver. The shaded blue areas represent the area-weighted frequency distributions of the MODIS surface albedo in the corresponding latitude bands (June–August 2025); they are shown for reference and do not enter the averaging.

Comment 11

Section 4.4: The goal of this section needs to be explained. It is unclear to me why the authors present the dependencies of Φ on the solar zenith angle and surface albedo are presented. What is the potential scientific use of this information?

Section 4.4 tests the adding model against the simulations and explains the use of Φ. The model predicts that Φ depends on SZA and the solver, but not on surface albedo; Fig. 4b confirms that Φ is independent of A_s. The closed-form forcing expression we added (Eq. 12) shows that, for $A_s < 1$, the ADRF is positive if and only if $A_s > 1/\Phi$. The curve Φ(SZA) in Fig. 4a therefore gives the critical surface albedo for positive forcing at every SZA (0.32 at 5°, 0.44 at 35° and 0.80 at 55° for DISORT). It also gives the SZA beyond which no surface is bright enough for positive forcing ($\Phi < 1$, SZA $\gtrsim 60°$) and expresses the two-stream error in a single number (a critical albedo of 0.50 instead of 0.32 at SZA = 5°). We added two sentences stating this goal at the start of Sect. 4.4.

Revised manuscript, lines 328–330:

Finally, subtracting E (Eq. 6) from the upward irradiance without the aerosol layer, $S(\mu)A_s$, gives the following closed-form expression for the ADRF of the non-absorbing layer:

$$\mathrm{ADRF} = S(\mu)\,\frac{(1-A_s)(R_{\uparrow}A_s - R_{\downarrow})}{1-R_{\uparrow}A_s} \qquad (12)$$

Revised manuscript, lines 331–335:

Equation (12) shows that, for $A_s < 1$, the ADRF is positive if and only if $A_s > R{\downarrow}/R{\uparrow} = 1/\Phi$. Here, R↓ measures the part of the direct beam that the layer reflects to space before the surface can absorb it. The quantity $R{\uparrow}A_s$ measures the part that the layer returns to the surface after the first surface reflection. The forcing is positive when the second exceeds the first. The critical surface albedo for positive forcing is therefore set by Φ alone. With R↓ and R↑ from Sect. 4.4, Eq. (12) reproduces the simulated ADRF of Fig. 1 to within 0.003 W m^{-2} at every surface albedo and SZA.

Revised manuscript, lines 359–361:

In this section, we test the adding model's predictions that Φ depends on solar geometry and the solver but is independent of surface albedo (Sects. 4.2 and 4.3). We also determine Φ(SZA), which sets the critical surface albedo 1/Φ for positive forcing (Eq. 12).

Revised manuscript, lines 377–381:

Because Φ does not depend on A_s, the curve Φ(SZA) in Fig. 4a gives the critical surface albedo 1/Φ at every SZA: 0.32 at SZA = 5°, 0.44 at 35° and 0.80 at 55° for DISORT. These values agree with the zero crossings of the simulated ADRF to within 0.002, and no positive forcing is possible where $\Phi < 1$ (SZA ≳ 60°). The two-stream value $\Phi \approx 2.0$ at SZA = 5° corresponds to a critical albedo of 0.50 instead of 0.32. This difference expresses the two-stream underestimate of the positive forcing in Fig. 1 in a single number.

Comment 12

Lines 314-315: Please explain the potential use of the parameter Φ for scientific studies.

The most direct use of Φ is that it makes the mechanism explicit in a single number. By Eq. (12), the sign of the forcing over a Lambertian surface depends only on surface albedo and Φ: for $A_s < 1$, the forcing is positive if and only if $R{\uparrow}A_s > R{\downarrow}$, i.e., if $A_s > 1/\Phi$. R↓ measures the part of the direct beam that the layer reflects to space before the surface can absorb it. $R{\uparrow}A_s$ measures the part that the layer returns to the surface after the first surface reflection. The revised Sects. 4.3, 4.4 and 5 state three uses of Φ. First, Φ(SZA), computed once for a layer, gives the critical surface albedo 1/Φ at every solar geometry. Second, for an optically thin layer and at a given wavelength, Φ depends only on the phase function of the particles (Eq. 15), so it characterizes a type of particle rather than a single case. Third, the check of R↑ in Sect. 4.4 makes Φ a test of how a radiative transfer scheme treats diffuse light. The two-stream scheme underestimates Φ because it underestimates the layer's reflectance for diffuse light.

Revised manuscript, lines 331–335:

Equation (12) shows that, for $A_s < 1$, the ADRF is positive if and only if $A_s > R{\downarrow}/R{\uparrow} = 1/\Phi$. Here, R↓ measures the part of the direct beam that the layer reflects to space before the

surface can absorb it. The quantity $R\uparrow A_s$ measures the part that the layer returns to the surface after the first surface reflection. The forcing is positive when the second exceeds the first. The critical surface albedo for positive forcing is therefore set by Φ alone. With $R\downarrow$ and $R\uparrow$ from Sect. 4.4, Eq. (12) reproduces the simulated ADRF of Fig. 1 to within 0.003 W m^{-2} at every surface albedo and SZA.

Revised manuscript, lines 351–352:

At a given wavelength, the optical depth and the single-scattering albedo cancel in Eq. (15). Particle size and composition therefore affect Φ only through the phase function.

Revised manuscript, lines 417–423:

Equation (12) shows that the forcing is positive wherever $1/\Phi < A_s < 1$. The model predicts that Φ should be independent of surface albedo – a prediction confirmed by numerical radiative transfer simulations (Fig. 4b). For any Lambertian surface, Φ therefore reduces the condition for positive forcing to a single number per solar geometry. The mechanism follows directly: the forcing is positive when the layer returns more of the surface-reflected light to the surface ($R\uparrow A_s$) than it reflects of the incoming solar beam to space ($R\downarrow$). Once computed for a given layer, Φ(SZA) gives the critical surface albedo for positive forcing at every solar geometry (0.32 at SZA = 5° for DISORT, 0.50 for RODENTS). The check of $R\uparrow$ in Sect. 4.4 also makes Φ a test of how a radiative transfer scheme treats diffuse light.

Comment 13

Lines 332-336: This text has no clear relation to the contents of the manuscript.

This paragraph addresses the weak absorption of real alumina, which the main simulations exclude by design. We rewrote its opening to explain the connection to the manuscript. At small SZA, surface-reflected light crosses the aerosol layer along oblique paths that are longer, on average, than the direct-beam path. Multiple reflections between the surface and layer make the light cross the layer repeatedly. Both effects lengthen its path inside the layer, so even weak absorption shifts the forcing toward positive values (Fig. S1).

Revised manuscript, lines 442–450:

The purely scattering case isolates the geometric mechanism, but measured alumina absorbs weakly, with an imaginary refractive index of the order of 10^{-4} (Kapoor et al., 2026). Light reflected by a bright surface is diffuse. It crosses the layer along oblique paths that are, on average, longer than the path of the direct beam at small SZA (Sect. 4.2). Multiple reflections between the surface and the layer also make the light cross the layer repeatedly. Both effects lengthen the photon path inside the layer, so even this weak absorption shifts the forcing toward positive values (Fig. S1): at SZA = 5°, by 0.09 W m^{-2} at $A_s = 0$ and by 0.70 W m^{-2} at $A_s = 1$. Combined with the scattering-induced ground absorption mechanism described here, even weak particle absorption due to defects (Kapoor et al., 2026) or impurities (Kumar et al., 2026) can further enhance positive TOA radiative forcing.

Revised Supplement, Fig. S1 and its caption:

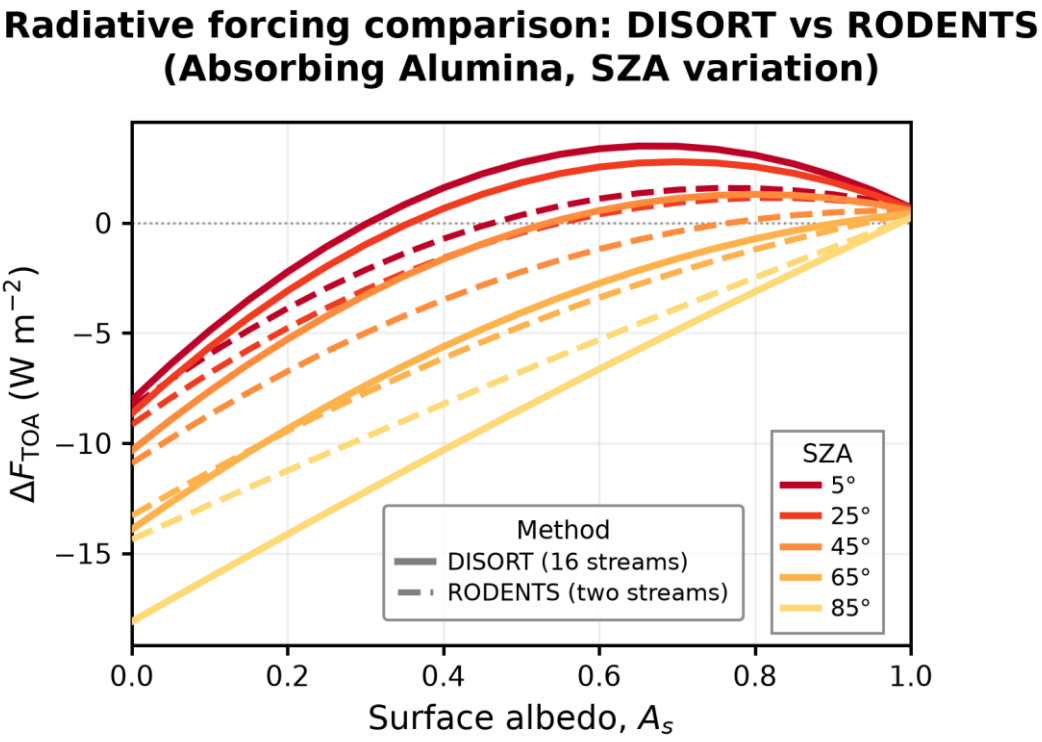


Figure S1. It illustrates the sensitivity of ADRF to surface albedo, SZA, and the multiple scattering treatment (DISORT vs. RODENTS) following the injection of alumina aerosols with imaginary part from Kapoor et al. (2026). Injected alumina follows the lognormal distribution with median diameter 430 nm, geometric standard deviation 1.5 and number concentration 11.3 cm^{-3}. The injection height is between 18 km and 24 km (stratosphere).

Technical corrections

Technical correction 1

Line 77: "independence to" → "independence of"

This correction has been made.

Revised manuscript, lines 76–80:

We test the robustness of this mechanism using the reflectance asymmetry parameter Φ, defined as the ratio of the layer's reflectance for diffuse light reflected by the surface to its reflectance for the direct beam (Sect. 4). Numerical radiative transfer simulations confirm that this parameter depends on solar geometry and is independent of the underlying surface albedo.

Technical correction 2

Line 92: The notation "#/cm^3" is quite weird, please use "particles/cm^3" instead

We changed the unit to cm^{-3} in Sect. 2.1 and the captions of Figs. 1 and S1, following the journal's convention of negative exponents for units. The word "particles" is implied by "number concentration". The value 11.3 replaces the rounded value 11 (Author-initiated corrections, item 4).

Revised manuscript, lines 95–98:

> We assumed a lognormal particle size distribution with a median diameter of 430 nm, a geometric standard deviation of 1.5, and a number concentration of 11.3 cm^{-3}. These parameters are similar to those used by Dykema et al. (2016) to produce radiative forcing of 1 W m^{-2} with alumina particles.

Revised manuscript, lines 162–165:

> **Figure 1.** Illustration of the sensitivity of ADRF to surface albedo, SZA, and the multiple scattering treatment (DISORT vs. RODENTS) following the injection of pure scattering alumina aerosols. Injected alumina follows the lognormal distribution with median diameter 430 nm, geometric standard deviation 1.5 and number concentration 11.3 cm^{-3}. The injection height is between 18 km and 24 km (stratosphere).

Revised Supplement, caption of Fig. S1:

> **Figure S1.** It illustrates the sensitivity of ADRF to surface albedo, SZA, and the multiple scattering treatment (DISORT vs. RODENTS) following the injection of alumina aerosols with imaginary part from Kapoor et al. (2026). Injected alumina follows the lognormal distribution with median diameter 430 nm, geometric standard deviation 1.5 and number concentration 11.3 cm^{-3}. The injection height is between 18 km and 24 km (stratosphere).

Technical correction 3

> *Line 110 and throughout the text: To avoid confusion please put spaces around dashes and use long dashes, e.g. "input to the RTE-extinction coefficient" → "input to the RTE – extinction coefficient"*

We replaced the unspaced parenthetical dashes with spaced en dashes, following the journal's style. Ranges use unspaced en dashes. Hyphens in compound words (e.g., two-stream) and en dashes joining two names (e.g., DISORT–RODENTS) are unchanged.

Revised manuscript, lines 48–50:

> Intercomparison studies have shown that differences in the treatment of multiple scattering among radiative transfer schemes contribute to 10–20 % discrepancies in modeled ADRF (Randles et al., 2013).

Revised manuscript, lines 120–122:

> We computed the aerosol optical properties required as input to the RTE – extinction coefficient, SSA, and scattering phase function – using Lorenz–Mie theory for homogeneous spherical particles, as implemented in the PyMieScatt Python library (Sumlin et al., 2018).

Revised manuscript, lines 191–194:

This pattern – two-stream methods overestimating cooling at low SZA and underestimating it at high SZA – is consistent with the findings of Randles et al. (2013), who compared 31 radiative transfer schemes with line-by-line benchmarks for a scattering aerosol over a surface of albedo 0.2.

Revised manuscript, lines 224–225:

The higher A_s values are uncommon at these latitudes, as shown in the blue shaded frequency distributions on the right y-axes in Fig. 2b–d.

Revised manuscript, lines 371–373:

At larger SZA, Φ falls below unity: R↓ exceeds R↑ (Fig. S3), and the layer reflects the direct beam more strongly than the diffuse upwelling light, consistent with the negative ADRF at high SZA (Figs. 1 and S2).

Revised Supplement, caption of Fig. S2:

Figure S2. This figure extends Fig. 1 of the main text to the high-SZA range 85–89°. At SZA > 85°, the magnitude of ADRF decreases and approaches zero as SZA approaches 90°. These results are indicative only because the plane-parallel geometry is not reliable for top-of-atmosphere fluxes at SZA > 85° (Sect. S5).

Revised Supplement, Sect. S2, list of assumptions of the single-layer adding model:

Two effective pairs: (R↓, T↓) for the collimated solar beam, slant path Δz/μ – hence μ-dependent; (R↑, T↑) for the diffuse upwelling field.

Revised manuscript, lines 509–511:

LZ: Methodology, Software, Formal Analysis, Writing – Original Draft; TSK: Validation, Writing – Review & Editing, Supervision; PU: Validation, Writing – Review & Editing; RKC: Conceptualization, Writing – Review & Editing, Supervision, Funding acquisition.

Technical correction 4

Section 4.2, title: the section title should be in bold face, "Radiation" → "radiation"

We corrected the title, which is now in bold face like the other subsection titles.

Revised manuscript, line 275:

4.2 Reflectance asymmetry between downwelling and upwelling radiation

Technical correction 5

Figure 4, caption: "As ," → "As,"

We corrected this.

Revised manuscript, lines 384–388:

Figure 4. Dependence of the reflectance asymmetry parameter Φ on SZA and surface albedo. (a) Φ as a function of SZA, illustrating the systematic bias between DISORT (solid) and RODENTS (dashed) solvers. (b) Φ as a function of surface albedo (A_s) for three

representative SZA values (5°, 45°, 85°). Note that Φ remains constant with respect to A_s, confirming the model prediction that reflectance asymmetry is independent of the underlying surface albedo.

Author-initiated corrections

While checking the model configuration for General Comment 1 of Reviewer 1, we compared the source data for every figure with the corresponding model input files. Some submitted figures used settings from an earlier stage of the work: a spectral band of 250–800 nm instead of 250–3000 nm and, for the SZA = 5° and 25° curves of Fig. 1, a Henyey–Greenstein test phase function with g = 0.7 instead of the Mie phase function. We reran all simulations for Figs. 1, 2, 4 and S1–S3 with the configuration stated in Sect. 2 (Mie optical properties from PyMieScatt, 250–3000 nm, DISORT with 16 streams and RODENTS) and replaced these figures. The conclusions are unchanged. The corrected reflectance asymmetry, peak forcing and difference between DISORT and RODENTS are larger. The following numbers in the text changed:

1. Section 3: the maximum instantaneous ADRF at SZA = 5° is +3.1 W m^{-2} at $A_s \approx 0.65$ (previously +2 W m^{-2} at $A_s = 0.6$). The zero crossing at SZA = 5° in Fig. 1 moves from $A_s \approx 0.23$ to $A_s \approx 0.32$. The SZA range in which DISORT gives a higher ADRF than RODENTS now reads 5–65°, at 65° only for $A_s \geq 0.2$ (previously 0–65°).

Revised manuscript, lines 173–176:

> However, at lower SZA (e.g., $\theta < 45°$) the sign of ADRF becomes more complicated: ADRF initially grows (less negative forcing) with increasing A_s, and crosses zero to become positive. It reaches a maximum (e.g., ADRF = +3.1 W m^{-2} at $\theta = 5°$, $A_s \approx 0.65$, using the DISORT solver), and then decreases to zero at $A_s = 1$. Positive ADRF indicates a net reduction in the flux reflected to space despite the aerosol being purely scattering.

Revised manuscript, lines 187–189:

> At SZA values between approximately 5° and 65° (at 65°, only for $A_s \geq 0.2$), DISORT yields higher (more positive) ADRF than RODENTS, meaning that the two-stream approximation underestimates the positive forcing in this regime.

Revised manuscript, Fig. 1 and its caption (lines 162–165):

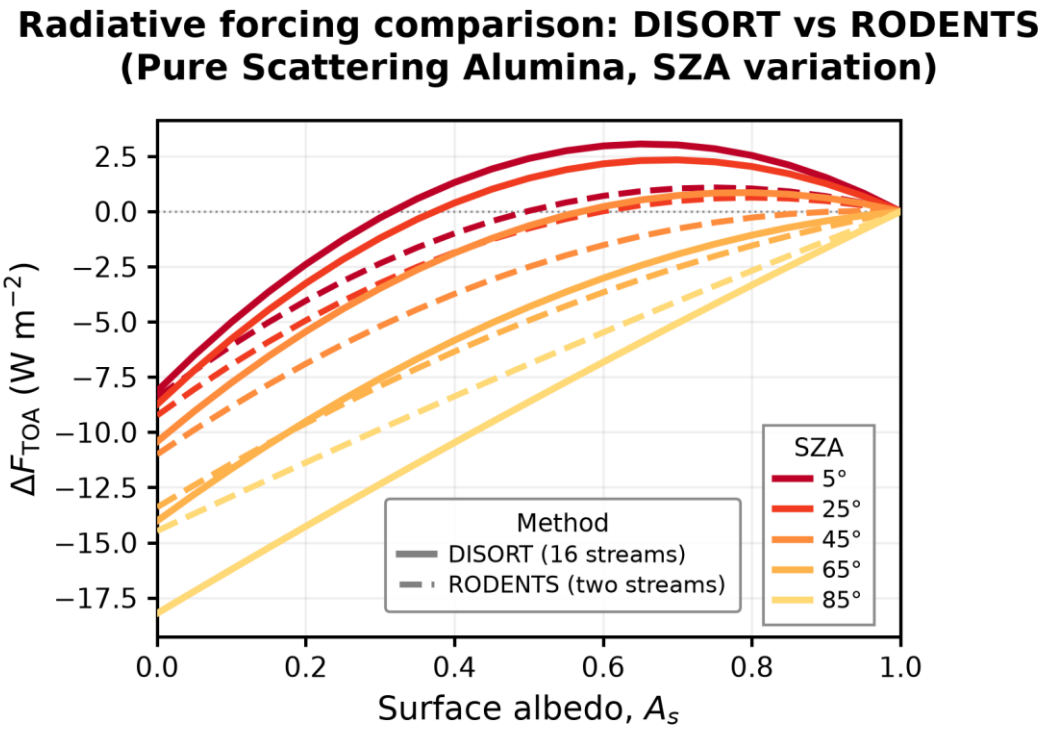


Figure 1. Illustration of the sensitivity of ADRF to surface albedo, SZA, and the multiple scattering treatment (DISORT vs. RODENTS) following the injection of pure scattering alumina aerosols. Injected alumina follows the lognormal distribution with median diameter 430 nm, geometric standard deviation 1.5 and number concentration 11.3 cm^{-3}. The injection height is between 18 km and 24 km (stratosphere).

2. Section 4.4: $\Phi \approx 3.2$ for DISORT at SZA = 5°. The previously quoted value of 2.0 was the RODENTS value, which remains ≈ 2.0. The $\Phi = 1$ crossover is at ≈ 60° for DISORT and at ≈ 48° for RODENTS (previously 55–60° and ≈ 45°).

Revised manuscript, lines 366–373:

Figure 4a shows Φ as a function of SZA for both DISORT and RODENTS. At low SZA, Φ is substantially greater than unity ($\Phi \approx 3.2$ for DISORT and $\Phi \approx 2.0$ for RODENTS at SZA = 5°), confirming that the layer reflects a much larger fraction of diffuse upwelling light than collimated downwelling light. As SZA increases, Φ decreases monotonically. It crosses unity near SZA ≈ 60° for DISORT, as expected from Eq. (15), and near 48° for RODENTS. At larger SZA, Φ falls below unity: R↓ exceeds R↑ (Fig. S3), and the layer reflects the direct beam more strongly than the diffuse upwelling light, consistent with the negative ADRF at high SZA (Figs. 1 and S2).

Revised manuscript, Fig. 4 and its caption (lines 384–388):

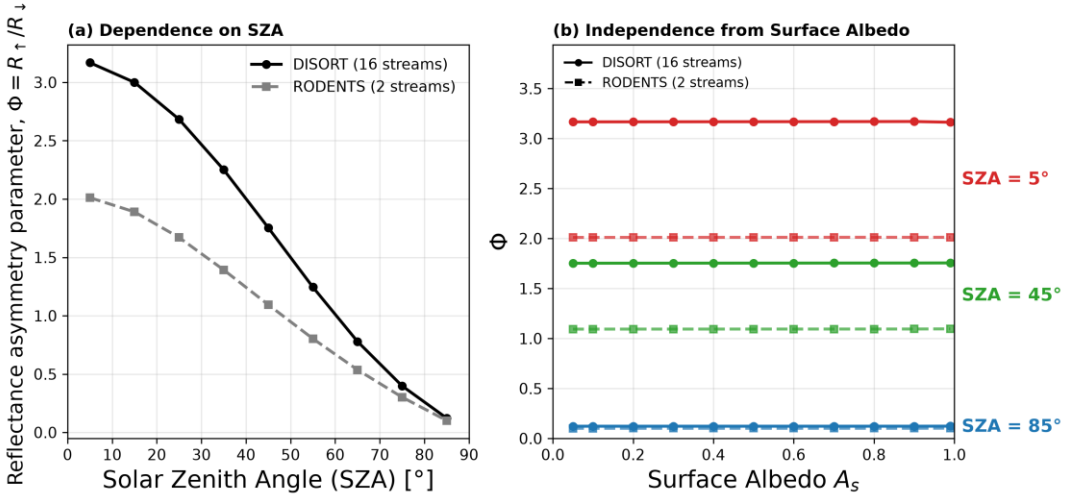


Figure 4. Dependence of the reflectance asymmetry parameter Φ on SZA and surface albedo. (a) Φ as a function of SZA, illustrating the systematic bias between DISORT (solid) and RODENTS (dashed) solvers. (b) Φ as a function of surface albedo (A_s) for three representative SZA values (5°, 45°, 85°). Note that Φ remains constant with respect to A_s, confirming the model prediction that reflectance asymmetry is independent of the underlying surface albedo.

3. Section 3: in the polar panel of Fig. 2, the reversal of the sign of the solver bias extends to $A_s \lesssim 0.4$ (previously ~0.2).

Revised manuscript, lines 226–228:

In the polar regions (Fig. 2d), the DISORT–RODENTS difference is further reduced, and at low albedos (A_s < ~0.4) the sign of the bias reverses; RODENTS yields slightly higher (less negative) ADRF than DISORT.

Revised manuscript, Fig. 2 and its caption (lines 204–211):

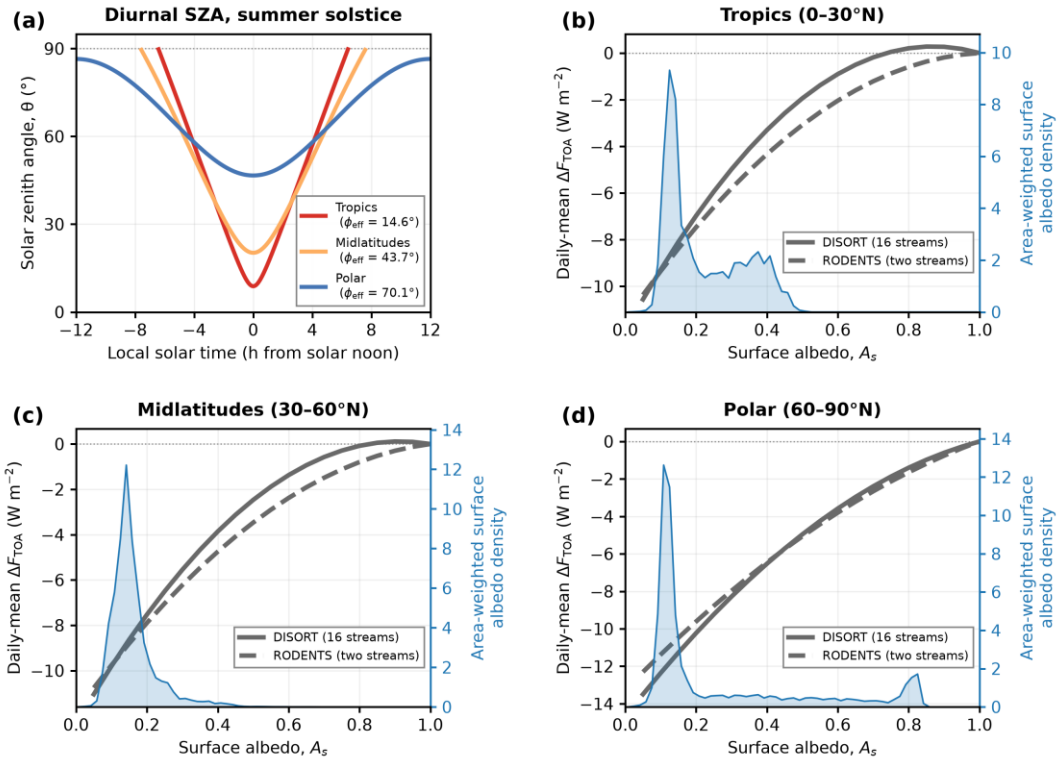


Figure 2. Daily-mean ADRF at the effective latitude of each latitude band, as a function of the prescribed uniform surface albedo A_s. The method for calculating this averaged ADRF is described in Sect. 2.3. Figure 2a shows the diurnal cycle of SZA for the three latitude bands; Fig. 2b, c and d respectively represent the daily-mean ADRF in the tropics, midlatitudes and polar region on the summer-solstice day in the northern hemisphere. The solid lines represent DISORT 16 streams solver and dashed lines represent RODENTS two streams solver. The shaded blue areas represent the area-weighted frequency distributions of the MODIS surface albedo in the corresponding latitude bands (June–August 2025); they are shown for reference and do not enter the averaging.

4. Section 2.1: the number concentration is stated as 11.3 cm^{-3} (previously rounded to 11), and the simulated SZA range is stated as 5–89°.

Revised manuscript, lines 95–98:

We assumed a lognormal particle size distribution with a median diameter of 430 nm, a geometric standard deviation of 1.5, and a number concentration of 11.3 cm^{-3}. These parameters are similar to those used by Dykema et al. (2016) to produce radiative forcing of 1 W m^{-2} with alumina particles.

Revised manuscript, lines 109–111:

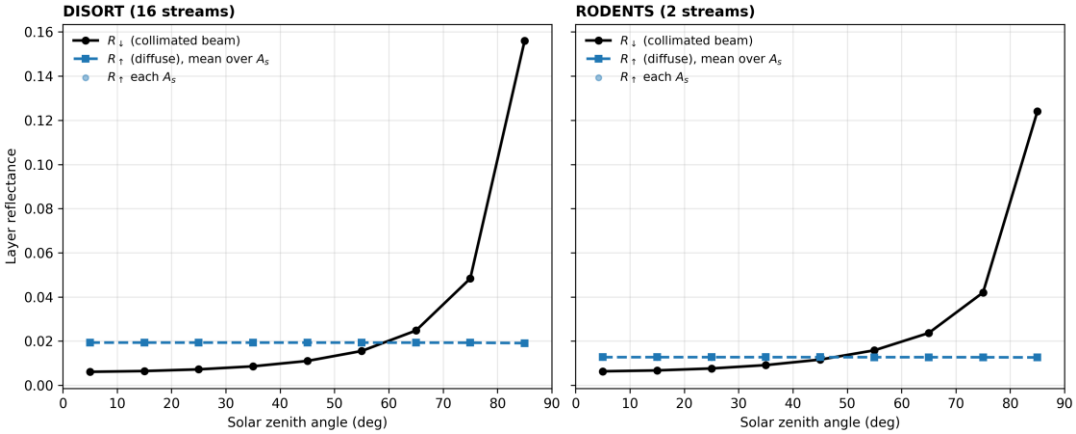
Simulations were performed across surface albedo values from 0 to 1 and SZA values from 5° to 89° to simulate plausible ranges of influence of diurnal and latitudinal changes to radiative forcing.

5. Section 4.4: R↑ is described as independent of surface albedo and constant to within about 1 % across SZA (previously "constant across both").

Revised manuscript, lines 362–364:

> The extracted reflectances are shown separately in Fig. S3: R↓ increases monotonically with SZA, reflecting the lengthening slant path of the collimated beam, whereas R↑ is independent of surface albedo and varies by less than about 1 % across SZA.

Revised Supplement, Fig. S3 and its caption:



> **Figure S3.** Downwelling and upwelling layer reflectances R↓ and R↑ as functions of solar zenith angle, extracted from the same simulations as Fig. 4 via Eqs. (10) and (11), for (a) DISORT (16 streams) and (b) RODENTS (2 streams). R↓ (black circles), the layer reflectance to the collimated solar beam, increases monotonically with SZA as the beam's slant path through the layer ($\propto 1/\cos\theta$) lengthens. R↑ (blue squares), the layer reflectance to the diffuse upwelling field, is shown as the mean over surface albedos $A_s \in [0.3, 0.95]$; light-blue points show the individual estimates extracted independently at each A_s, which coincide at every SZA. R↑ is independent of A_s and varies by less than about 1 % across SZA, consistent with the model assumption that the upwelling field incident on the layer base is isotropic and therefore carries no memory of the solar geometry. Estimates at small A_s are excluded from the mean because Eq. (11) is ill-conditioned as $A_s \to 0$. The SZA-dependence of Φ in Fig. 4a therefore originates entirely in R↓; the crossing R↓ = R↑ marks $\Phi = 1$.

6. Section 3: with the regenerated Fig. 2, the daily-mean ADRF computed with DISORT becomes positive only at $A_s \geq 0.74$ in the tropics and $A_s \geq 0.83$ at midlatitudes, and it remains at or below zero in the polar band (previously "$A_s > \sim 0.8$", with such values described as rare outside polar regions).

Revised manuscript, lines 217–220:

> With DISORT, the daily-mean ADRF becomes positive only at very high surface albedo ($A_s \geq 0.74$ in the tropics and $A_s \geq 0.83$ at midlatitudes), and such values are rare in these bands. In the polar band, the daily-mean ADRF remains at or below zero at every surface albedo.

We also made the following corrections:

A1. The aerosol layer extended from 18 to 24 km in all calculations, rather than 18–23 km as stated in the submitted text. The six 1 km aerosol layers beginning at 18–23 km occupy 18–24 km. We corrected the stated altitude range; the calculated results are unchanged because the simulations already used this configuration.

Revised manuscript, lines 93–94:

> The injected aerosol layer was placed between 18 km and 24 km altitude, corresponding to the lower stratosphere where proposed SAI deployment would occur (Dykema et al., 2016; Weisenstein et al., 2015).

Revised manuscript, lines 162–165:

> **Figure 1.** Illustration of the sensitivity of ADRF to surface albedo, SZA, and the multiple scattering treatment (DISORT vs. RODENTS) following the injection of pure scattering alumina aerosols. Injected alumina follows the lognormal distribution with median diameter 430 nm, geometric standard deviation 1.5 and number concentration 11.3 cm^{-3}. The injection height is between 18 km and 24 km (stratosphere).

A2. We added the missing space after "June–August 2025." in Sect. 3 (the submitted text read "2025.In").

Revised manuscript, lines 225–226:

> Surface albedo distributions were derived from the MODIS MCD43 BRDF/Albedo product (Schaaf and Wang, 2021), averaged over June–August 2025.

A3. The Fig. 4 caption and one sentence in the Conclusions used "reflectance ratio parameter"; both now read "reflectance asymmetry parameter", the term used throughout the text.

Revised manuscript, lines 384–388:

> **Figure 4.** Dependence of the reflectance asymmetry parameter Φ on SZA and surface albedo. (a) Φ as a function of SZA, illustrating the systematic bias between DISORT (solid) and RODENTS (dashed) solvers. (b) Φ as a function of surface albedo (A_s) for three representative SZA values (5°, 45°, 85°). Note that Φ remains constant with respect to A_s, confirming the model prediction that reflectance asymmetry is independent of the underlying surface albedo.

Revised manuscript, lines 415–417:

> We defined a reflectance asymmetry parameter $\Phi = R\uparrow/R\downarrow$ that quantifies this asymmetry and showed analytically that, at fixed R↓, increasing Φ reduces the TOA reflected flux for $0 < A_s < 1$ (Eq. 9).

A4. The Danabasoglu et al. (2020) entry now gives the full list of 43 authors, as ACP requires complete author lists.

Revised manuscript, reference list (lines 536–542):

> Danabasoglu, G., Lamarque, J.-F., Bacmeister, J., Bailey, D. A., DuVivier, A. K., Edwards, J., Emmons, L. K., Fasullo, J., Garcia, R., Gettelman, A., Hannay, C., Holland, M. M.,

Large, W. G., Lauritzen, P. H., Lawrence, D. M., Lenaerts, J. T. M., Lindsay, K., Lipscomb, W. H., Mills, M. J., Neale, R., Oleson, K. W., Otto-Bliesner, B., Phillips, A. S., Sacks, W., Tilmes, S., van Kampenhout, L., Vertenstein, M., Bertini, A., Dennis, J., Deser, C., Fischer, C., Fox-Kemper, B., Kay, J. E., Kinnison, D., Kushner, P. J., Larson, V. E., Long, M. C., Mickelson, S., Moore, J. K., Nienhouse, E., Polvani, L., Rasch, P. J., and Strand, W. G.: The Community Earth System Model Version 2 (CESM2), J. Adv. Model. Earth Sy., 12, e2019MS001916, https://doi.org/10.1029/2019MS001916, 2020.

A5. We added the missing volume number of Kumar et al. (2026) (J. Aerosol Sci., 194, 106767).

Revised manuscript, reference list (lines 573–574):

Kumar, J., Jung, G. Y., Kapoor, T. S., Mishra, R., and Chakrabarty, R. K.: Strong light absorption by sp2 hybridized carbon impurities in diamond dust, J. Aerosol Sci., 194, 106767, https://doi.org/10.1016/j.jaerosci.2026.106767, 2026.

A6. The daily SZA weighting for Fig. 2 had been computed for 1 June, whereas the caption states the summer solstice. We regenerated the figure for 21 June. The date change alone has a minor effect on the figure and affects no conclusion. The daily-mean ADRF in Fig. 2b and c is larger in magnitude than in the submitted figure because these panels had been computed for 250–800 nm, whereas Fig. 2d already used 250–3000 nm.

A7. Section 2.1 and the captions of Figs. 1 and S1 called the 430 nm parameter of the lognormal distribution the "mean diameter". This parameter is the median (geometric mean) diameter of the number distribution, and the text now reads "median diameter".

Revised manuscript, lines 95–98:

We assumed a lognormal particle size distribution with a median diameter of 430 nm, a geometric standard deviation of 1.5, and a number concentration of 11.3 cm^{-3}. These parameters are similar to those used by Dykema et al. (2016) to produce radiative forcing of 1 W m^{-2} with alumina particles.

Revised Supplement, caption of Fig. S1:

Figure S1. It illustrates the sensitivity of ADRF to surface albedo, SZA, and the multiple scattering treatment (DISORT vs. RODENTS) following the injection of alumina aerosols with imaginary part from Kapoor et al. (2026). Injected alumina follows the lognormal distribution with median diameter 430 nm, geometric standard deviation 1.5 and number concentration 11.3 cm^{-3}. The injection height is between 18 km and 24 km (stratosphere).

A8. The submitted text cited Maloney et al. (2025) and Robock et al. (2008), which were missing from the reference list; both entries have been added.

Revised manuscript, reference list (lines 577–579 and 602–603):

Maloney, C. M., Portmann, R. W., Ross, M. N., and Rosenlof, K. H.: Investigating the potential atmospheric accumulation and radiative impact of the coming increase in satellite reentry frequency, J. Geophys. Res.-Atmos., 130, e2024JD042442, https://doi.org/10.1029/2024JD042442, 2025.

Robock, A., Oman, L., and Stenchikov, G. L.: Regional climate responses to geoengineering with tropical and Arctic SO_2 injections, J. Geophys. Res., 113, D16101, https://doi.org/10.1029/2008JD010050, 2008.

A9. Abstract: "bright surfaces such as snow and ice" now reads "bright surfaces such as snow and desert". The phrase "through the layer and is preferentially backscattered to the surface" now reads "through the aerosol layer and is preferentially backscattered to the ground". The phrase "may underestimate the localized climatic risks" now reads "may underestimate localized climatic risks".

Revised manuscript, lines 11–12:

This study investigates the counter-intuitive positive shortwave radiative forcing induced by purely scattering aerosols over bright surfaces such as snow and desert.

Revised manuscript, lines 17–19:

We introduce the reflectance asymmetry parameter (Φ) to quantify this asymmetry: diffuse upwelling light encounters a longer optical path through the aerosol layer and is preferentially backscattered to the ground.

Revised manuscript, lines 20–22:

These findings suggest that current assessments may underestimate localized climatic risks of SAI and extend to any optically thin scattering layer over bright surfaces – including the growing burden of reentry-derived alumina.

A10. Supplement, Eq. (S7): we corrected a typographical error in the range of t_{hours} ([−12.12) → [−12, 12)).

Revised Supplement, Sect. S2, Eq. (S7):

$$h(t) = 15^{\circ} \cdot t_{hours},\ t_{hours} \in [-12, 12) \qquad \text{(S7)}$$

A11. Supplement, Sects. S1 and S2: we corrected three typographical errors in the equations. In Eq. (S2), the sum now runs over the moment index l and includes the factor (2l + 1)/2; P_l now takes $\mu_i = \cos\theta_i$ instead of θ_i. In Eq. (S3), the trapezoidal sum now uses $(\mu_i - \mu_{i+1})$ because μ_i decreases with i. In Sect. S2, λ in the area element is the longitude, not the latitude.

Revised Supplement, Sect. S1, Eq. (S2):

$$P_{\text{Mie}}(\theta_i) \approx \sum_{l=0}^{32} \frac{2l+1}{2} k_l P_l(\mu_i), \quad \text{with} \quad \mu_i = \cos\theta_i \qquad \text{(S2)}$$

Revised Supplement, Sect. S1, Eq. (S3):

$$k_l = \int_{-1}^{1} P_{\text{Mie}}(\mu) P_l(\mu) \mathrm{d}\mu \approx \sum_{i=0}^{N-1} \frac{1}{2} [P_{\text{Mie}}(\mu_i) P_l(\mu_i) + P_{\text{Mie}}(\mu_{i+1}) P_l(\mu_{i+1})](\mu_i - \mu_{i+1}) \qquad \text{(S3)}$$

Revised Supplement, Sect. S2, text after Eq. (S6):

One can treat ϕ_{eff} as the cosine-area-weighted mean latitude (It's a standard way in climate data averaging because the surface-area element on a sphere is $dA = R^2 \cos\phi\, d\phi\, d\lambda$, λ is longitude).

A12. We corrected "Hartmann et al., 2016" to "Hartmann, 2016" because the book has a single author. We also replaced the reference to the preprint of Kapoor et al. (2026) with the published article in Geophysical Research Letters, in both the manuscript and the Supplement.

Revised manuscript, lines 473–474:

> Clouds possess high albedo (0.4–0.9 depending on thickness, water content, and type) (Hartmann, 2016) and reside at altitudes (2–12 km) below the modeled SAI injection height.

Revised manuscript, reference list (lines 568–572), and revised Supplement, reference list:

> Kapoor, T. S., Upadhyay, P., Huang, J., Ren, G., Cavin, J., Mitroo, D., Vattioni, S., Dykema, J., Sedlacek, J., Kumar, J., Hachtel, J. A., Xu, L., Mishra, R., and Chakrabarty, R. K.: Unveiling the shortwave absorption spectra of alumina aerosols: radiative implications for solar radiation modification, Geophys. Res. Lett., 53, e2026GL121668, https://doi.org/10.1029/2026GL121668, 2026.

A13. We corrected three statements that did not match the equations or figures. Section 2.1 described the ADRF as the change in net upward flux, whereas its defining equation gives the change in net downward flux. Section 4.3 stated that increasing Φ lowers the radiative forcing, whereas Eq. (9) shows that it raises the ADRF. The opening of Sect. 4 cited Fig. 2b for the lower SZA at low latitudes, which is shown in Fig. 2a. The sentence of the Conclusions quoted under A3 now also states that Eq. (9) applies at fixed $R\downarrow$ and for $0 < A_s < 1$.

Revised manuscript, lines 116–117:

> The ADRF is then defined as the change in net downward shortwave flux at the TOA due to the presence of the aerosol layer:

Revised manuscript, line 318:

> Thus, increasing Φ lowers E (and raises the ADRF) for $0 < A_s < 1$.

Revised manuscript, lines 247–249:

> Regions where low SZA coincides with high surface albedo – such as low-latitude deserts, salt flats, and snow-covered mountains – are therefore susceptible to this mechanism (Fig. 2a).

References

Anderson, G. P., Clough, S. A., Kneizys, F. X., Chetwynd, J. H., and Shettle, E. P.: AFGL atmospheric constituent profiles (0–120 km), Tech. Rep. AFGL-TR-86-0110, Air Force Geophysics Laboratory, Hanscom Air Force Base, Bedford, Massachusetts, USA, 1986.

Brownlee, D. E., Ferry, G. V., and Tomandl, D.: Stratospheric aluminum oxide, Science, 191, 1270–1271, https://doi.org/10.1126/science.191.4233.1270, 1976.

Danabasoglu, G., Lamarque, J.-F., Bacmeister, J., Bailey, D. A., DuVivier, A. K., Edwards, J., Emmons, L. K., Fasullo, J., Garcia, R., Gettelman, A., Hannay, C., Holland, M. M., Large, W. G., Lauritzen, P. H., Lawrence, D. M., Lenaerts, J. T. M., Lindsay, K., Lipscomb, W. H., Mills, M. J., Neale, R., Oleson, K. W., Otto-Bliesner, B., Phillips, A. S., Sacks, W., Tilmes,

S., van Kampenhout, L., Vertenstein, M., Bertini, A., Dennis, J., Deser, C., Fischer, C., Fox-Kemper, B., Kay, J. E., Kinnison, D., Kushner, P. J., Larson, V. E., Long, M. C., Mickelson, S., Moore, J. K., Nienhouse, E., Polvani, L., Rasch, P. J., and Strand, W. G.: The Community Earth System Model Version 2 (CESM2), J. Adv. Model. Earth Sy., 12, e2019MS001916, https://doi.org/10.1029/2019MS001916, 2020.

Dykema, J. A., Keith, D. W., and Keutsch, F. N.: Improved aerosol radiative properties as a foundation for solar geoengineering risk assessment, Geophys. Res. Lett., 43, 7758–7766, https://doi.org/10.1002/2016GL069258, 2016.

Emde, C., Buras-Schnell, R., Kylling, A., Mayer, B., Gasteiger, J., Hamann, U., Kylling, J., Richter, B., Pause, C., Dowling, T., and Bugliaro, L.: The libRadtran software package for radiative transfer calculations (version 2.0.1), Geosci. Model Dev., 9, 1647–1672, https://doi.org/10.5194/gmd-9-1647-2016, 2016.

Ferreira, J. P., Huang, Z., Nomura, K., and Wang, J.: Potential ozone depletion from satellite demise during atmospheric reentry in the era of mega-constellations, Geophys. Res. Lett., 51, e2024GL109280, https://doi.org/10.1029/2024GL109280, 2024.

Hartmann, D. L.: Global Physical Climatology, 2nd edn., Elsevier, Amsterdam, the Netherlands, https://doi.org/10.1016/C2009-0-00030-0, 2016.

Kapoor, T. S., Upadhyay, P., Huang, J., Ren, G., Cavin, J., Mitroo, D., Vattioni, S., Dykema, J., Sedlacek, J., Kumar, J., Hachtel, J. A., Xu, L., Mishra, R., and Chakrabarty, R. K.: Unveiling the shortwave absorption spectra of alumina aerosols: radiative implications for solar radiation modification, Geophys. Res. Lett., 53, e2026GL121668, https://doi.org/10.1029/2026GL121668, 2026.

Kumar, J., Jung, G. Y., Kapoor, T. S., Mishra, R., and Chakrabarty, R. K.: Strong light absorption by sp2 hybridized carbon impurities in diamond dust, J. Aerosol Sci., 194, 106767, https://doi.org/10.1016/j.jaerosci.2026.106767, 2026.

Maloney, C. M., Portmann, R. W., Ross, M. N., and Rosenlof, K. H.: Investigating the potential atmospheric accumulation and radiative impact of the coming increase in satellite reentry frequency, J. Geophys. Res.-Atmos., 130, e2024JD042442, https://doi.org/10.1029/2024JD042442, 2025.

Mishchenko, M. I., Travis, L. D., Kahn, R. A., and West, R. A.: Modeling phase functions for dustlike tropospheric aerosols using a shape mixture of randomly oriented polydisperse spheroids, J. Geophys. Res., 102, 16831–16847, https://doi.org/10.1029/96JD02110, 1997.

Murphy, D. M., Abou-Ghanem, M., Cziczo, D. J., Froyd, K. D., Jacquot, J., Lawler, M. J., Maloney, C., Plane, J. M. C., Ross, M. N., Schill, G. P., and Shen, X.: Metals from spacecraft reentry in stratospheric aerosol particles, P. Natl. Acad. Sci. USA, 120, e2313374120, https://doi.org/10.1073/pnas.2313374120, 2023.

Pierluissi, J. H. and Peng, G.-S.: New molecular transmission band models for LOWTRAN, Opt. Eng., 24, 541–547, https://doi.org/10.1117/12.7973523, 1985.

Randles, C. A., Kinne, S., Myhre, G., Schulz, M., Stier, P., Fischer, J., Doppler, L., Highwood, E., Ryder, C., Harris, B., Huttunen, J., Ma, Y., Pinker, R. T., Mayer, B., Neubauer, D., Hitzenberger, R., Oreopoulos, L., Lee, D., Pitari, G., Di Genova, G., Quaas, J., Rose, F. G.,

Kato, S., Rumbold, S. T., Vardavas, I., Hatzianastassiou, N., Matsoukas, C., Yu, H., Zhang, F., Zhang, H., and Lu, P.: Intercomparison of shortwave radiative transfer schemes in global aerosol modeling: results from the AeroCom Radiative Transfer Experiment, Atmos. Chem. Phys., 13, 2347–2379, https://doi.org/10.5194/acp-13-2347-2013, 2013.

Ricchiazzi, P., Yang, S., Gautier, C., and Sowle, D.: SBDART: A research and teaching software tool for plane-parallel radiative transfer in the Earth's atmosphere, B. Am. Meteorol. Soc., 79, 2101–2114, https://doi.org/10.1175/1520-0477(1998)079<2101:SARATS>2.0.CO;2, 1998.

Robock, A., Oman, L., and Stenchikov, G. L.: Regional climate responses to geoengineering with tropical and Arctic SO_2 injections, J. Geophys. Res., 113, D16101, https://doi.org/10.1029/2008JD010050, 2008.

Schaaf, C. and Wang, Z.: MODIS/Terra+Aqua BRDF/Albedo Albedo Daily L3 Global 0.05Deg CMG V061, NASA Land Processes Distributed Active Archive Center [data set], https://doi.org/10.5067/MODIS/MCD43C3.061, 2021.

Stamnes, K., Tsay, S.-C., Wiscombe, W., and Jayaweera, K.: Numerically stable algorithm for discrete-ordinate-method radiative transfer in multiple scattering and emitting layered media, Appl. Optics, 27, 2502–2509, https://doi.org/10.1364/AO.27.002502, 1988.

Sumlin, B. J., Heinson, W. R., and Chakrabarty, R. K.: Retrieving the aerosol complex refractive index using PyMieScatt: a Mie computational package with visualization capabilities, J. Quant. Spectrosc. Ra., 205, 127–134, https://doi.org/10.1016/j.jqsrt.2017.10.012, 2018.

Tropf, W. J. and Thomas, M. E.: Aluminum oxide (Al2O3) revisited, in: Handbook of Optical Constants of Solids, edited by: Palik, E. D., Academic Press, 653–682, https://doi.org/10.1016/B978-012544415-6.50124-2, 1997.

Vattioni, S., Weber, R., Feinberg, A., Stenke, A., Dykema, J. A., Luo, B., Kelesidis, G. A., Bruun, C. A., Sukhodolov, T., Keutsch, F. N., Peter, T., and Chiodo, G.: A fully coupled solid-particle microphysics scheme for stratospheric aerosol injections within the aerosol–chemistry–climate model SOCOL-AERv2, Geosci. Model Dev., 17, 7767–7793, https://doi.org/10.5194/gmd-17-7767-2024, 2024.

Weisenstein, D. K., Keith, D. W., and Dykema, J. A.: Solar geoengineering using solid aerosol in the stratosphere, Atmos. Chem. Phys., 15, 11835–11859, https://doi.org/10.5194/acp-15-11835-2015, 2015.

Wiscombe, W. J.: The delta-M method: rapid yet accurate radiative flux calculations for strongly asymmetric phase functions, J. Atmos. Sci., 34, 1408–1422, https://doi.org/10.1175/1520-0469(1977)034<1408:TDMRYA>2.0.CO;2, 1977.

Zdunkowski, W., Trautmann, T., and Bott, A.: Radiation in the Atmosphere: A Course in Theoretical Meteorology, Cambridge University Press, Cambridge, UK, 2007.